ELSEVIER

Journal of Hazardous Materials A67 (1999) 41–58

Journal of Hazardous Materials

Heat transfer in large-scale heavy-gas dispersion

Morten Nielsen *, Søren Ott

Risø National Laboratory, P.O. Box 49, DK-4000 Roskilde, Denmark

Received 12 September 1998; received in revised form 15 September 1998; accepted 1 February 1999

Abstract

Heavy-gas dispersion of practical interest is usually cold gas dispersion with the enthalpy deficit as the main cause of the density effect. New analysis of existing field experiment data suggests that heat transfer from the ground sometimes reduces this thermally induced density effect considerably. The limited heat capacity of the ground implies that heat transfer to a gas plume must disappear eventually, and our interpretation of Desert Tortoise measurements indicates that the surface heat flux decreased by 38% during a 3-min long release period.

Keywords: Heavy-gas dispersion; Heat transfer; Enthalpy

1. Introduction

Large quantities of gas are normally stored in liquid form in pressurized or refrigerated containers. Accidental release results in flash boiling jets or cold liquid pools. In either case the evaporating vapour will be colder than the ambient air, and for many gases the density effect caused by the temperature deficit will be comparable to that of the molar weight difference. If the gas is mixed with ambient air in an adiabatic process, the cloud buoyancy would be nearly conserved [1] for mixtures diluted sufficiently to preclude liquid aerosols. In the adiabatic case a carefully chosen isothermal simulation gas provides a good wind-tunnel model of the density-to-concentration correlation of a cold large-scale release.

Is adiabatic mixing a realistic assumption? In the non-isothermal laboratory experiments of Meroney and Neff [2] surface heat transfer was found to reduce the excess

* Corresponding author. Tel.: +45-4677-5022; Fax: +45-4677-5970; E-mail: n.m.nielsen@risoe.dk

[1] The cloud buoyancy would be *exactly* conserved if the molar specific heats of the contaminant and air were identical. This is a good approximation for molecules of the same structure [1].

0304-3894/99/$ - see front matter
PII: S0304-3894(99)00016-3

density. These authors even observed a cold and initially heavy methane plume lift off the ground at the downwind distance where heat transfer from the wind-tunnel floor had made the plume buoyant. Ruff et al. [3] measured the heat balance of a cold nitrogen gravity current and identified heat transfer from the wind tunnel floor as the main cause of the depth-integrated buoyancy change. The dynamic effect of this was clearly demonstrated by the experiments of Gröbelbauer [4] who studied a similar gravity current advancing over a surface with controllable temperature, and the front velocity was observed to slow down when the heat transfer was turned on. Britter [5] reviewed the scaling laws for simultaneous heavy-gas dispersion and surface heat transfer and concluded that additional constraints had to be imposed on the thermal diffusivity and heat capacity of the simulant gas in the limit of forced convection. He found that free convection was impossible to model correctly. These scaling-law difficulties were also recognized by Meroney and Neff [2] who estimated that heat transfer effects should be weaker though probably still significant in full-scale releases in the atmosphere. Heat transfer effects have not yet been accurately quantified in full scale and are often ignored. Kunsch and Fanneløp [6] recently found and experimentally verified an analytical solution for simultaneous heat transfer and gravitational spreading in a calm environment. The significant transfer mechanism in an emission of cryogenic gas (LNG) was identified as free convection. With a well insulated surface the cloud heating was intensified in the region just behind the advancing front of the cloud where the ground surface temperature under the cloud decreased substantially.

2. Theory

The objective of the present paper is to examine the significance and time dependence of heat transfer in large-scale heavy-gas dispersion. For simplicity we chose to test a ‘null statement’ of the question of significance, by tentatively assuming that mixing is adiabatic and then seeing if the heat budget can be balanced. By a similar simplistic approach, the local cloud temperature is regarded as constant in a surface-cooling model, although possible time-dependence of the heat flux obviously would affect local temperature.

2.1. Heat budget for adiabatic mixing

Consider a homogeneous mixture of gas, aerosols and ambient air in thermodynamical equilibrium. In case of *negligible heat input* from the surroundings the mixture enthalpy is related to the source enthalpy by:

$$\overbrace{(T - T_{\text{air}}) \cdot \left[(1 - c) \cdot M_{\text{air}} c_p^{\text{air}} + c \cdot M c_p\right] + \Delta H_{\text{con}}}^{\Delta H} = c \cdot \Delta H_0 \tag{1}$$

Here $T - T_{\text{air}}$ is the temperature deficit [°C], (c_p, c_p^{air}) and (M, M_{air}) are the heat capacities [J (kg °C)$^{-1}$] and molar weights of contaminant and air [kg mol^{-1}], ΔH_{con}

accounts for the enthalpy deficit [J mol^{-1}] of condensed matter including air humidity and c is the concentration [mol mol^{-1}]. The left-hand side of Eq. (1) is the mixture enthalpy deficit ΔH [mol mol^{-1}] relative to ambient conditions, so the entrained air does not contribute to this. The released material contributes ΔH_0 [mol mol^{-1}] defined as the enthalpy difference between the contaminant at source and ambient conditions. When the material evaporates from the liquid phase, ΔH_0 is negative. In the non-adiabatic case the right-hand side of the equation could be written as $c(\Delta H_0 + Q)$ where Q would be the accumulated heat input per mole of contaminant. We tentatively disregard that contribution. Following Webber et al. [7], we model the heat of condensation term ΔH_{con} by

$$\Delta H_{con} = \alpha_{gas} cML + \alpha_{H_2O} q(1-c) M_{H_2O} L_{H_2O} + \alpha \Delta H_{mix} \quad (2)$$

where α_{gas} and α_{H_2O} [mol mol^{-1}] are degrees of condensation for contaminant and ambient water vapour, q [mol mol^{-1}] is the water vapour concentration in the entrained air, $\alpha = \alpha_{gas} c + \alpha_{H_2O} q(1-c)$ is the overall liquid fraction, L and L_{H_2O} are heats of evaporation [J kg^{-1}] and ΔH_{mix} is heat of chemical reaction in the liquid phase. The second term on the right-hand side is the contribution by condensation of ambient water vapour, which generally dominates the other terms. The degrees of condensation are hard to measure directly. When evaluating the condensation term we have to rely on the hypothesis of homogeneous thermal and vapour-pressure equilibrium of the aerosol fraction. Kukkonen et al. [8] considered a binary water/ammonia aerosol ventilated by its fall velocity and concluded that the assumption of homogeneous equilibrium provides sufficiently accurate predictions of the cloud temperature and density for aerosol diameters less than 100 μm. Equilibrium vapour pressures for hygroscopic aerosols are most accurately modelled by binary-aerosol models—here we apply the model of Wheatley [9] also summarized by Nielsen et al. [10]. For contaminants other than ammonia (propane, LNG) we simply consider the phase-equilibrium of water.

It could be argued that a kinetic energy term should be included in Eq. (1) and indeed such a term plays an important role in two-phase pipe flow models [11]. The ratio of the jet momentum to the release rate $F_{jet}/\dot{m}$ can be taken as an upper limit for the jet velocity. In the FLADIS liquefied ammonia experiments [10] this was ≈ 70 m s^{-1}, and the corresponding kinetic energy of 2.5 kJ kg^{-1} was insignificant compared to the 1270 kJ kg^{-1} heat of evaporation. This justifies our neglect of kinetic energy terms in Eq. (1) when determining mixture temperatures. Assuming an aerosol Weber number equal to 12, the estimated jet velocity corresponds to an initial aerosol radius equal to ≈ 16 μm, i.e. sufficiently small to allow the homogeneous equilibrium assumption.

2.2. Mixture density

The density of a dry mixture of air and gas at modest pressure is found by the ideal gas law

$$\rho = \frac{P_{air}\left[Mc + M_{air}(1-c) \right]}{RT} \quad (3)$$

where P_{air} is the pressure and R is the universal gas constant. By inserting Eq. (1) without the condensation term, we obtain the following formula valid in the case of *dry adiabatic mixing*:

$$\frac{\Delta\rho}{\rho_{\text{air}}} = \frac{M_{\text{air}} + c\Delta M}{M_{\text{air}} + \dfrac{cM_{\text{air}}c\Delta H_0}{\left[(1-c)M_{\text{air}}c_p^{\text{air}} + cMc_p\right]T_{\text{air}}}} - 1 \approx c\left\{\frac{\Delta M}{M_{\text{air}}} - \frac{\Delta H_0}{M_{\text{air}}c_p^{\text{air}}T_{\text{air}}}\right\} \quad (4)$$

The linearization is justified since in most cases the gas is swiftly diluted by near-source entrainment, i.e. $c \ll 1$. The density effect of an enthalpy deficit is seen to be equivalent to excess molar weight and consequently we define an 'effective' molar weight by

$$M_{\text{eff}} = M - \Delta H_0 / c_p^{\text{air}} T_{\text{air}}. \quad (5)$$

This can be used for scaling isothermal wind tunnel simulations of two-phase releases—still assuming *dry adiabatic mixing*.

2.3. Source enthalpy

Accurate values of ΔH_0, the enthalpy deficit between released material at exit conditions and at ambient temperature, can be obtained from thermodynamic tables. It is instructive to consider the following estimate:

$$\Delta H_0 \approx -\overbrace{\alpha \cdot ML}^{\text{evaporation}} - \overbrace{Mc_p \cdot (T_{\text{air}} - T_{\text{exit}})}^{\text{mixing}} - \overbrace{f \cdot (1-f)^{-1} Mc_p' \cdot (T_{\text{rain}} - T_{\text{exit}})}^{\text{rainout}} \quad (6)$$

Here T_{exit} and T_{rain} are temperatures of the gas source and rained out aerosols, f is the mass fraction of rain-out aerosols and c_p' is heat capacity of the released material in liquid phase. The rain-out fraction f is here taken relative to the total mass including the rained out material, whereas the liquid mass fraction α is relative to the airborne mass only. Eq. (6) consists of three contributions: (1) the heat of evaporation of the airborne liquid; (2) the heat associated with a possible source temperature difference and (3) an adjustment applied to correct for liquid rain-out. The argument for the latter is that if the rain-out mass fraction f is cooled before it separates from the mixture, that heat will be absorbed in the remaining $1-f$ mass fraction of the release. The temperature of the rained-out material can be equal to the boiling point or lower, as observed in flash boiling jets [10]. For simplicity the rained out material is assumed to separate completely from the cloud so the evaporation of aerosols rained out on the ground is neglected. The exit conditions for pool sources are evaluated just after evaporation, i.e., the liquid mass fraction is set to *zero* and the exit temperature is that of the pool boundary layer. We ignore the fact that the thermodynamic properties L, c_p, and c_p' are functions of temperature. This error is reduced when the latent heat and heat capacities are evaluated at exit temperature T_{exit} and at average temperature $(T_{\text{air}} + T_{\text{exit}})/2$, respectively.

2.4. Heat transfer from ground to gas cloud

We simplify heat transfer in the ground to conduction in a homogeneous material of initial uniform temperature. The heat diffusion is then described by

$$\rho_{\text{soil}} c_{\text{soil}} \frac{\partial T(z,t)}{\partial t} = \lambda_{\text{soil}} \frac{\partial^2 T(z,t)}{\partial z^2} \tag{7}$$

where ρ_{soil} [kg m^{-3}], c_{soil} [J (kg °C)$^{-1}$] and λ_{soil} [W (m °C)$^{-1}$] are the soil density, specific heat and thermal conductivity and z [m] is the depth into soil. The upward heat flux (opposite to the chosen z direction) is proportional to the temperature gradient

$$\varphi(z,t) = \lambda_{\text{soil}} \frac{\partial T(z,t)}{\partial z} \tag{8}$$

The heat transfer from the surface of the ground to the gas cloud is described by forced heat convection

$$\varphi(0,t) = \rho_{\text{gas}} c_p c_{\text{h}} u\big(T(0,t) - T_{\text{gas}}\big) \tag{9}$$

where ρ_{gas} [kg m^{-3}] and c_p [J (kg °C)$^{-1}$] are the density and specific heat of the gas cloud, c_{h} is a non-dimensional heat transfer coefficient, u is the cloud velocity [m s^{-1}], and $T(0,t) - T_{\text{gas}}$ is the temperature difference [°C] between the surface and the gas mixture. In practice the transfer process will often be a combination of forced and free convection causing the heat transfer coefficient c_{h} to change as a function of the developing cloud temperature [6]. However, for simplicity we shall regard c_{h} and the local cloud temperature T_{gas} as constant.

The mathematical solution to the above equations is given in Appendix A. It predicts how, after sudden exposure to a cold gas layer, the temperature drop gradually penetrates from the surface into the soil. This transient model will enable us to estimate the surface heat flux $\varphi(0,t)$ from heat-flux data measured below the surface $\varphi(z,t)$. The measuring position of the available data is not accurately known but it will be estimated by a comparison of measured and calculated time series.

3. Analysis

3.1. Selected data

From the REDIPHEM database [12] we have selected information from trials EEC55 and EEC57 of the MTH project BA propane experiments, DT3 of the Desert Tortoise ammonia experiments and B8 of the Burro LNG experiment. Our criteria for this selection were to cover a range of source types and gases, to apply data from well exposed instruments, to apply data from steady continuous releases and to have detailed background information. References to the chosen experiments and characterisations of the selected time series are presented in Table 1. For the analysis we need pairs of adjacent temperature and concentration signals from well-exposed locations near the

Table 1
Overview of field data

	MTH BA	Desert tortoise	Burro
Reference	Nielsen [13] Heinrich and Scherwinski [14] Nielsen and Jensen [21]	Koopman et al. [19] Goldwire et al. [17]	Koopman et al. [16] Koopman et al. [20]
Distances	38 and 63 m	100 and 800 m	57, 140, 400 and 800 m
Concentration	Kaijo-Denki[a]	LLNL-IR[b] (100 m) IST[c] (800 m)	LLNL-IR[b] (57, 140 m) IST[c] (400, 800 m)
Temperature	Thermocouples	Thermocouples	Thermocouples
Heat-flux	–	HY-CAL[d]	–

[a] Sonic anemometer with attached thermocouple.
[b] Non-dispersive infrared absorption sensor.
[c] Solid state sensor.
[d] Thermopile.

plume centreline. We find such information from four distances in the Burro experiment and two distances in the other experiments. From the Desert Tortoise experiment, we include heat-flux signals from thermopile devices (HY-CAL) placed next to each mast just beneath the surface.

All temperature measurements were made by relatively fast responding thermocouples. The concentration signals from the MTH BA experiments were deduced from the gas-induced distortion of the sound virtual temperature signals of ultrasonic anemometers (Kaijo-Denki) relative to the true temperature detected by attached thermocouples—this technique is described by Nielsen [13]. The response time of the derived signal is as fast as that of the thermocouples, i.e., about 1 s. In the Burro and Desert Tortoise experiments the gas was detected by a combination of fast responding, about 1 s, infrared absorption sensors developed by Lawrence Livermore National Laboratory (LLNL-IR) and slower, about 15 s, solid state concentration sensors from International Sensor Technology (IST). The sample gas was passed through a heater to evaporate all aerosols before concentration measurement.

The source types are shown in Fig. 1. The source in EEC55 was a horizontal nozzle pointing in the downwind direction with an exit pressure sufficiently high to fragment the liquid propane into a mist of tiny fully airborne aerosols. Following the arguments at the end of Section 2.1, we estimate the initial aerosol radius in EEC55 to ≈ 7 μm. In

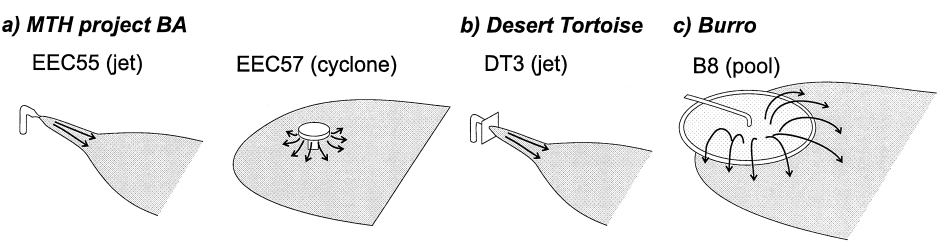

Fig. 1. Sketch of gas sources in the selected trials.

EEC57 the liquid was depressurized inside a cyclone source in order to provide a gas release with no net momentum. The discharge was in all horizontal directions and covered an area upstream of the release point. Approximately one third of the released material was deposited inside the cyclone and spilled into a liquid pool on the ground [14]. This implies that the liquid fraction of the emitted material was different from that of the nozzle. The temperature of the material rained-out in the cyclone is unknown. We assume that it was close to the atmospheric boiling point since the gas concentration inside the cyclone must have been $\approx 100\%$ and the pressure close to 1 Bar. The source in DT3 passed through a vertical 'spill plate' with an orifice facing the downwind direction. This source had no nozzle contraction and produced a horizontal jet with some liquid rain out. The data report describes extensive pool formation (2000 m^2) but estimates the overall flow-rate reduction to be 'modest'. In lack of detailed information we subjectively assume that this produced a rain-out fraction of $f \approx 5\%$. In the Burro experiment liquid LNG was spilled on a water pond with a diameter of 57 m. The water was an efficient heat supply and the LNG boiled instantly. Differential boil-off of the LNG compounds seems likely, and we assume that the initial boil-off composition in the B8 trial was pure methane. Only data from the initial stages of this trial have been used, i.e. the first one and a half minute of data at each measuring station. The solid-state IST sensors were calibrated for methane detection and were sensitive to variable LNG composition—another reason to avoid the final stages of the pool evaporation. In the MTH BA experiments a 2 m high fence was mounted perpendicular to the centre-line at $x = 48$ m between the two measuring positions. This fence was removed in the middle of the gas releases in order to determine its influence on the dispersion process. Release conditions including meteorological conditions and references to detailed descriptions are summarized in Table 2. The source enthalpy deficits ΔH_0 are found as differences between the contaminant at exit and ambient conditions looked up in the tables of Vargaftik [15], with a correction for liquid rain out calculated by the last term in Eq. (6).

3.2. Heat budgets

Fig. 2 shows time series of concentration and temperature measured by adjacent sensors. The ambient temperature T_{air} is represented by a time series from an unexposed reference thermocouple at the top of the front mast. In order to adjust the pre-trial enthalpy deficit to zero, the temperature signal was corrected for its pre-trial difference relative to the reference thermometer. The water content of the air q_{air} was calculated by upwind measurements of the relative humidity. The reference signal was low-pass filtered leaving only the general trend of the ambient temperature. The time response of the other signals were matched by moving average filters. The enthalpy time series shown at the bottom of the figure was then calculated by the left-hand side of Eq. (1). The enthalpy contributions by the liquid aerosols ΔH_{con} varied, as discussed in Appendix B. Judged from the figure the calculated in situ enthalpy appears to correlate with gas concentration.

Fig. 3 shows scatter plots of 10-s block-average values of enthalpy and concentration. According to our 'null-statement' of adiabatic mixing we would expect ΔH equal to $c\Delta H_0$, see Eq. (1), so that the points should lie on a straight line, which they indeed

Table 2
Overview of release conditions

Trial	EEC55	EEC57	DT3	B8
Gas	propane	propane	ammonia	LNG[a]
Release type	jet	cyclone	jet	pool
Nozzle diameter	0.0155	–	0.095	–
Jet momentum, F_{jet} [kN]	≈ 0.25	–	≈ 11.4	–
Liquid fraction, α	1	1	1	0
Rain-out mass fraction, f	0	≈ 0.33	≈ 0.05	0
Exit temperature, T_{exit} [K]	287	287	295	≈ 111
Exit pressure, p_{exit} [Bar]	10.0	9.3	11.2	0.94
Source enthalpy, ΔH_0 [kJ mol^{-1}]	−16.3	−13.3	−21.4	−6.7
Release rate, $\dot{m}$ [kg s^{-1}]	3.0	3.0	133	≈ 115
Windspeed, u [m s^{-1}] at z [m]	3.2 at 6 m	2.4 at 6 m	7.4 at 2 m	1.8 at 2 m
Friction velocity, u_* [m s^{-1}]	≈ 0.19	≈ 0.16	0.45	0.074
Surface roughness, z_0 [mm]	6	6	3	0.25
Monin-Obukov length, L_{MO} [m]	≈ −90	≈ −20	570	16
Stability class	≈ D	≈ C	D	F
Cloud cover [%]	100	75	70	?
Ambient temperature, T_{air} [K]	283	287	307	306
Ambient pressure, P_{air} [hPa]	1025	1025	907	941
Relative humidity [%]	99	93	15	4.5

[a] LNG composition: 87% methane, 10% ethane and 2% propane.
Some parameters, e.g. the jet momentum F_{jet}, were evaluated in the REDIPHEM project [12].

seem to do. However, we shall demonstrate that the slopes of these lines are inconsistent with adiabatic mixing. Estimates of local $\Delta H/c$ ratios are obtained by linear regression lines of the type $c = \beta \times \Delta H$, by regression lines forced through the point $(c,\Delta H) = (0,0)$. The results of similar analyses for all selected signal pairs are plotted in Fig. 4. The first three diagrams contain estimates for two observation heights and the MTH BA experiments contain estimates from periods with and without an obstacle. Uncertainties are evaluated by the residual variance between observations and regression lines. This is actually just a lower bound on the uncertainty since some variance was removed by signal smoothing. The enthalpy to concentration ratios corresponding to adiabatic mixing (the source enthalpies) are indicated by dashed horizontal lines. For the Desert Tortoise and Burro experiments with low molar weight gases, we also include the enthalpy to concentration ratio where according to Eq. (5) the effective molar weight M_{eff} becomes equal to the molar weight of the ambient air. This is the limit where the initially dense plumes would be changed into buoyant ones by continued heating.

The observations of $\Delta H/c$ in all but the pool evaporation experiment lie significantly above the release condition and demonstrate that mixing was *not* adiabatic. The observation height and the presence of obstacles in the MTH BA experiments did not significantly influence the enthalpy to concentration ratio, i.e. the non-adiabatic heat input per contaminant concentration appeared to be height independent. In the two jet releases the enthalpy increased with downward distance and we interpret this as a result of accumulated heat transfer to the plume from the ground.

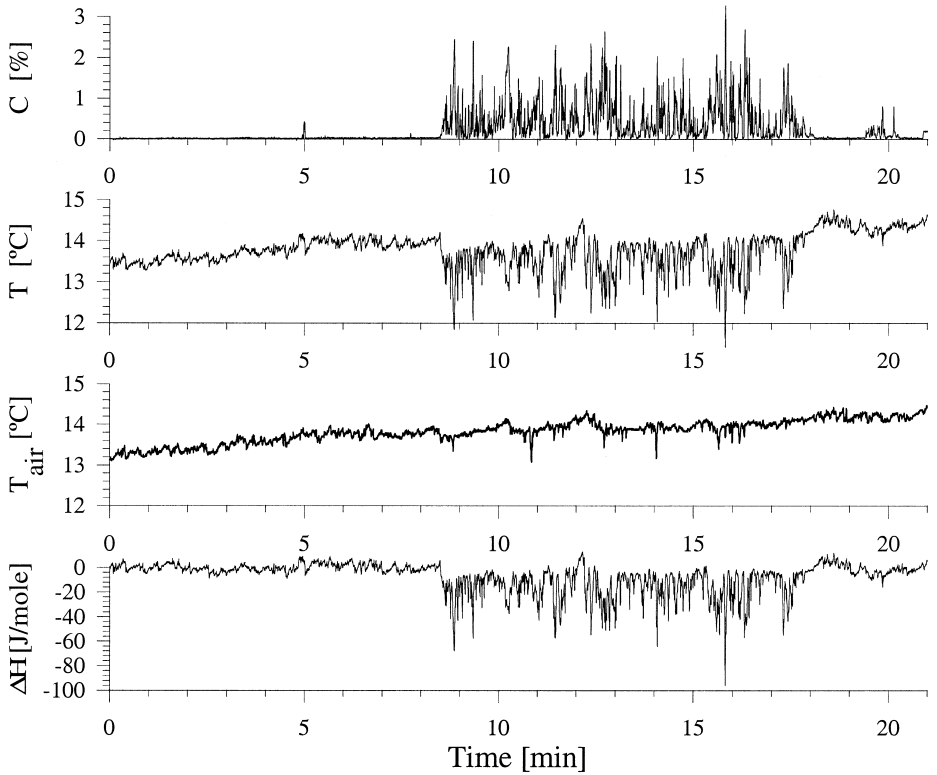

Fig. 2. EEC57, front mast, 1 m above terrain: Time series of concentration and temperature, ambient temperature and the derived enthalpy time series.

The release rates and meteorological conditions were comparable in the two MTH BA experiments so their differences in enthalpy to concentration ratios must relate to the sources. The near-source entrainment was most efficient with a jet release and presumably the jet was warmer than the plume when it first touched the ground. In addition the ground contact area upwind of the measuring positions was smaller for the jet than for the plume, see Fig. 1. In other words: the heating depends on the initial dispersion and thereby on source parameters such as momentum.

The absolute uncertainty of enthalpy to concentration ratios from the Burro experiment is comparable to those of the other experiments but the narrower range of possible enthalpy ratios makes the precision inadequate. We cannot conclude much from this experiment except that field observations indicated a warmer plume than the estimate from source enthalpy. The analysis of Koopman et al. [16] showed that the plume did not become buoyant.

Table 3 shows the influence on the 'effective' molar weight M_{eff} as defined by Eq. (5) with the release enthalpy substituted by the observed enthalpy to concentration ratios. The far-field effect of the density difference between cloud and ambient air $\Delta\rho$, after aerosol evaporation, is evaluated by Eq. (4). This is the key parameter in heavy-gas

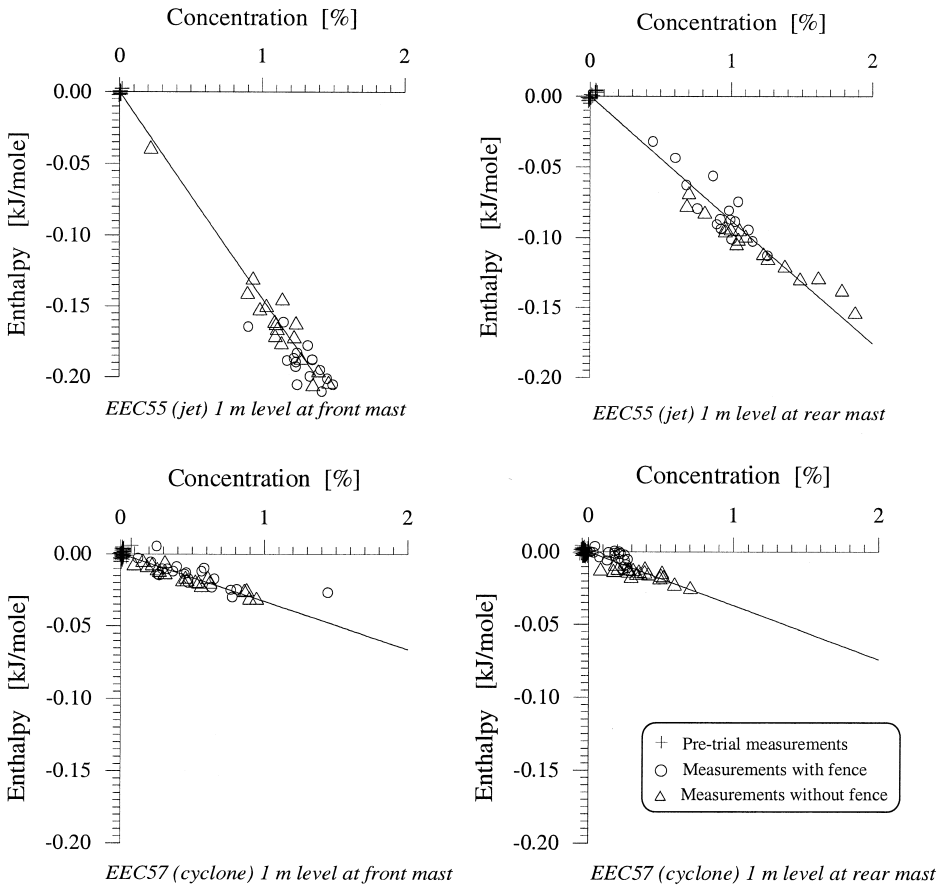

Fig. 3. Local correlations between 10-s block averages of enthalpy and concentration. The regression lines are forced through $(c,\Delta H)=(0,0)$.

dispersion and the magnitude of these thermally induced buoyancy reductions is significant—as predicted by Kunsch and Fanneløp [6].

3.3. Heat transfer from the ground

We are now ready to examine the heat flux from the soil and in particular whether this remains constant during the dispersion process. Fig. 5 shows the heat-flux signal from the sensor placed in the soil near the mast at 100 m distance in DT3 and the temperature and concentration 1 m above the ground. The sensors at 100-m distance were exposed approximately 40 sec after the beginning of the release equal to the start of the time axis. The concentration and temperature were almost constant in the period indicated by the shaded area. The ground heat-flux signal responded with a short time delay relative to the temperature signal and kept rising during the period of steady gas exposure. Based on remarks in the data report [17] and the smoothness of the heat flux time series, we believe that the ground was not flooded by the pool or covered with ice

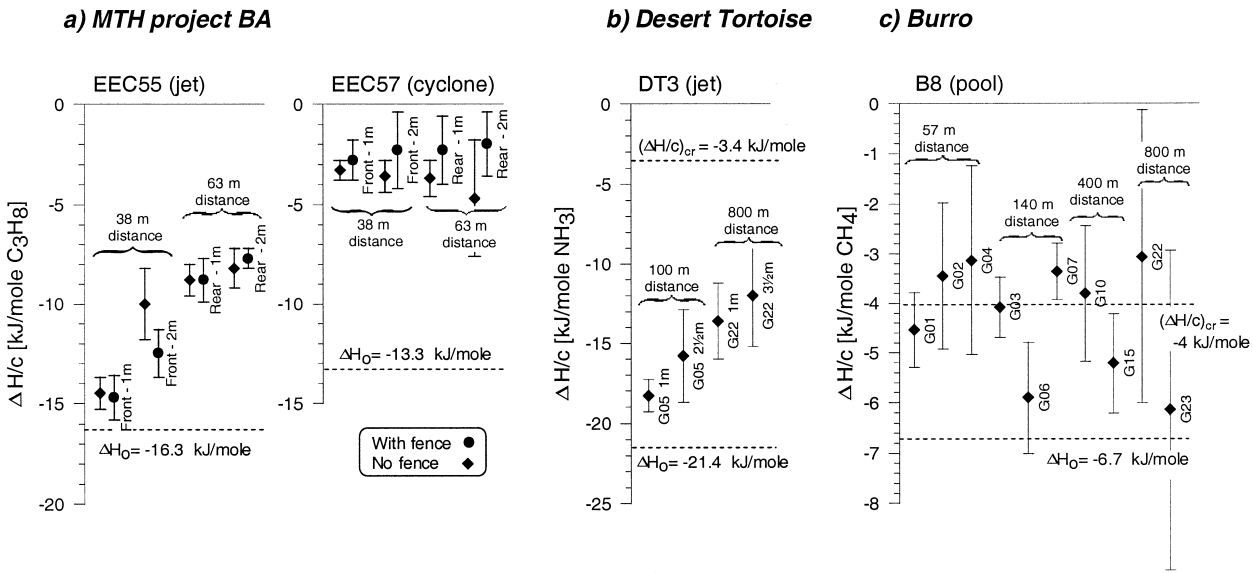

Fig. 4. Observed enthalpy to concentration ratios. Limits are included for 1) adiabatic mixing with the estimated source conditions ΔH_0 and 2) neutral buoyancy $(\Delta H/c)_{cr}$.

Table 3
Estimates of 'effective' molar weights M_{eff} at source and in the field and corresponding bouyancy reductions

	Source	In-field		$\Delta\rho$ reduction by heat transfer
EEC55	110 g mol^{-1}	78 g mol^{-1} (38 m)	68 g mol^{-1} (63 m)	40–52%
EEC57	98 g mol^{-1}	57 g mol^{-1}		59%
DT3	87 g mol^{-1}	77 g mol^{-1} (100 m)	61 g mol^{-1} (800 m)	17–38%

deposits at this distance. It is relevant therefore to compare the measured heat-flux signal with the model in Section 2.4 and its solution in Appendix A. The soil properties needed for the model are estimated to $\lambda_{soil} = 0.5$ W (m K)$^{-1}$, $c_{soil} = 1.8$ kJ (kg K)$^{-1}$ and $\rho_{soil} = 2000$ kg m^{-3} and numerical tests show that the solution is not very sensitive to the exact values of these.

The dashed curves in Fig. 5 are three solutions corresponding to initial surface heat fluxes of $\varphi_0 = 1250$, 1500, and 1750 kW m^{-2}, respectively. These curves are fixed by the heat flux at the end of the gas exposure and they are determined by an iteration of the unknown sensor depth, see Appendix A. The solution obtained with the median value of the surface heat flux $\varphi_0 = 1500$ kW m^{-2} is in overall agreement with the observations and predicts reasonably well the time delay relative to the gas exposure. It corresponds to a sensor depth of $z = 4.1$ mm.

The calculations are also shown by the dashed curves in Fig. 6 in the Appendix A. This figure presents the solution in a non-dimensional form. In Fig. 6 the curve corresponding to $\varphi_0 = 1500$ kW m^{-2} is the one ending on the non-dimensional release

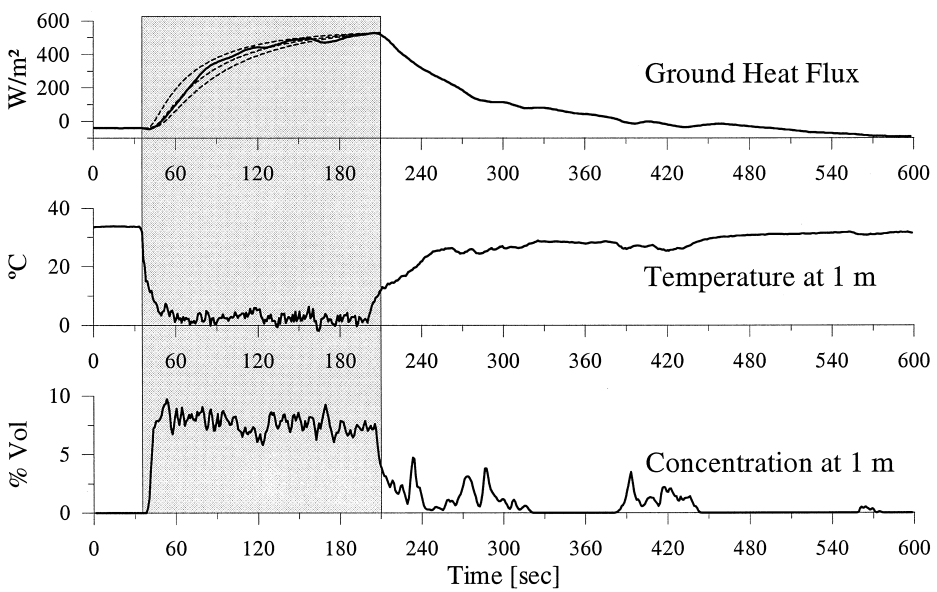

Fig. 5. DT3 100 m from source at the ideal plume centreline. Heat flux just below the surface together with temperature and concentration time series at 1 m.

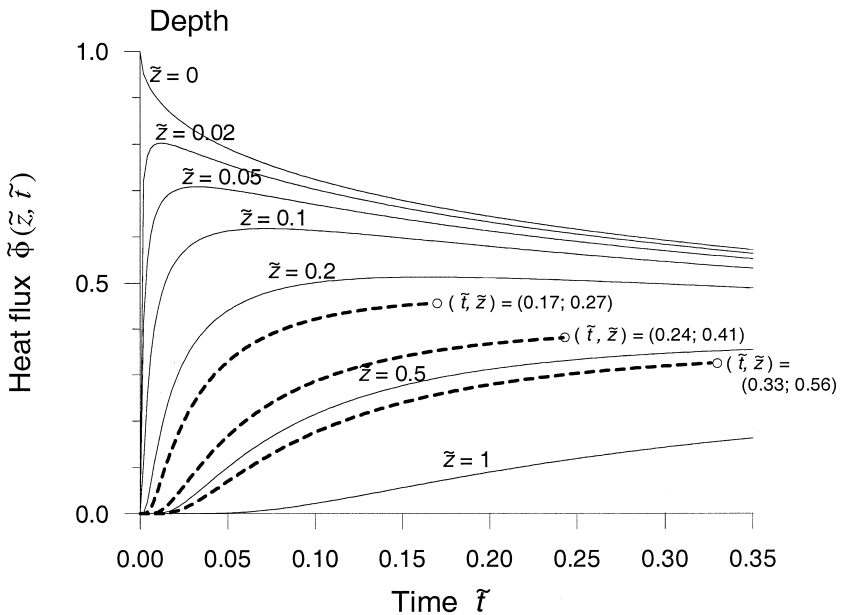

Fig. 6. Non-dimensional soil heat flux after sudden surface cooling as a function of time and depth.

duration $\tilde{t} = 0.24$. The model predicts that at this stage the surface heat flux has decreased to 62% of the initial heat-flux φ_0. Thus, in spite of the relatively short release duration in DT3, the heat flux from the ground was *not* constant.

4. Conclusions

The accumulated heat input from a warm ground to a cold heavy gas cloud has a noticeable effect on cloud density. The effect was particularly significant for the cyclone release mechanism in EEC57 which allowed the gas layer to cover a large area without much initial entrainment. The effect will be most significant when the major contribution to the cloud density is the source enthalpy rather than the contaminant molar weight. Large-scale heavy-gas dispersion experiments are sometimes intercompared with wind tunnel simulations in which the cloud density is produced by an isothermal model gas. The problem of this method is that the ‘effective’ molar weight of the large-scale dispersion gradually decreases in the downwind direction because surface heat transfer warms the plume. Sometimes the ‘effective’ molar weight is reduced by more than a factor of 2 compared to the ideal case of adiabatic mixing.

The heat transfer to the gas cloud is time dependent. Our analysis of heat-flux measurements at 100-m distance in trial DT 3 suggests that the surface heat flux decreased by 38% during that experiment. A consequence of a time dependent heat flux is that even with perfectly steady release and wind a non-isothermal heavy-gas dispersion would be time-varying at a given downwind position.

Kunsch and Fanneløp [6] previously predicted that heat transfer from the ground has a significant effect on cloud buoyancy. These authors applied a theoretical model and verified it by laboratory data. We have shown that the heat flux effect is significant also in large-scale experiments.

Large-scale liquefied-gas dispersion data often lack precise source measurements. The present analysis would benefit from better information on source enthalpy, i.e. initial temperature, phase composition and possible rain out. The source enthalpy ΔH_0 should be regarded as an important parameter in heavy-gas dispersion problems.

Acknowledgements

The MTH BA experiments were part of the project *Research on Continuous and Instantaneously Heavy Gas Clouds* (1988–1990) sponsored by the CEC DG XII Major Technological Hazards (MTH) programme. Steve Hanna communicated data from the Burro (1980) and Desert Tortoise experiment (1983) conducted by the Lawrence Livermore National Laboratory for U.S. Department of Energy and the U.S. Coast Guard. The Rediphem project (1992–1995) was sponsored by the CEC DG XII STEP programme. David Wilson made helpful comments on the manuscript.

Appendix A

The heat transfer problem defined in a Section 2.4 can be written in non-dimensional form

$$\frac{\partial \Delta\tilde{T}}{\partial \tilde{t}} = \frac{\partial^2 \Delta\tilde{T}}{\partial \tilde{z}^2}, \quad \tilde{\varphi} = \frac{\partial \tilde{T}}{\partial \tilde{z}}, \quad \text{and } \tilde{\varphi}(0,\tilde{t}) = \Delta\tilde{T}(0,\tilde{t}) \tag{A.1}$$

with the non-dimensional temperature deficit, depth, time and flux defined by

$$\begin{aligned} \Delta\tilde{T} &= \left(T(z,t) - T_{\text{gas}}\right)\left(\Delta T_0\right)^{-1} \\ \tilde{z} &= z\varphi_0\left(\lambda_{\text{soil}}\Delta T_0\right)^{-1} \\ \tilde{t} &= t\varphi_0^2\left(\rho_{\text{soil}} c_{\text{soil}} \lambda_{\text{soil}} \Delta T_0^2\right)^{-1} \\ \tilde{\varphi} &= \varphi \cdot \varphi_0^{-1} \end{aligned} \tag{A.2}$$

by using the initial surface heat flux

$$\varphi_0 = \lim_{t \to 0_+} \varphi(0,t)$$

and the initial ground temperature deficit $\Delta T_0 = T(z,0) - T_{\text{gas}}$.

The response to sudden forcing at the surface of the form

$$\begin{aligned} \Delta\tilde{T}(\tilde{z},\tilde{t}) &= 0 \qquad\qquad \text{for } \tilde{t} \le 0 \\ \Delta\tilde{T}(0,\tilde{t}) &= \sum_{n=0}^{\infty} a_n \tilde{t}^{n/2} \qquad \text{for } \tilde{t} > 0 \end{aligned} \tag{A.3}$$

where n is a positive natural number is given by Carslaw and Jaeger [18]. With these boundary conditions the temperature development becomes

$$\Delta\tilde{T}(\tilde{z},\tilde{t}) = \sum_{n=0}^{\infty} a_n 2^n \Gamma(n/2+1)\tilde{t}^{n/2} \times I^n \mathrm{erfc}\left(\frac{1}{2}\tilde{z}\tilde{t}^{-1/2}\right) \tag{A.4}$$

where the last factor is a shorthand notation for n integrations over the complementary error function

$$I^n \mathrm{erfc}(x) = \begin{cases} -2/\sqrt{\pi}\exp(-x^2) & \text{for } n=-1 \\ 2/\sqrt{\pi}\int_x^{\infty}\exp(-\xi^2)\mathrm{d}\xi & \text{for } n=0 \\ \int_x^{\infty} I^{n-1}\mathrm{erfc}(\xi)\mathrm{d}\xi & \text{for } n\geq 1 \end{cases} \tag{A.5}$$

The symbol 'I' refers to the integral operator $\int_x^{\infty}\mathrm{d}\xi$. The integrals can be found by the recursion formula:

$$I^n \mathrm{erfc}(x) = \left[I^{n-2}\mathrm{erfc}(x) - 2xI^{n-1}\mathrm{erfc}(x)\right]/2n \tag{A.6}$$

which is useful in proof of Eq. (A.4). For $x=0$ it can be shown that:

$$I^n \mathrm{erfc}(0) = \left[2^n \Gamma(n/2+1)\right]^{-1}. \tag{A.7}$$

Combining Eqs. (A.1) and (A.4) we find the coefficients

$$a_n = \begin{cases} 0 & \text{for } n=0 \\ (-1)^{n+1}\left[\Gamma(n/2+1)\right]^{-1} & \text{for } n\geq 1 \end{cases} \tag{A.8}$$

and the non-dimensional heat flux becomes:

$$\tilde{\varphi}(\tilde{z},\tilde{t}) = \sum_{n=0}^{\infty}(-2)^n \tilde{t}^{n/2} I^n \mathrm{erfc}\left(\frac{1}{2}\tilde{z}\tilde{t}^{-1/2}\right). \tag{A.9}$$

This solution is plotted by the thin solid lines in Fig. 6. Although not needed for our computations it may be of general interest to know that the time dependent surface flux $\tilde{\varphi}(0,\tilde{t})$ has an analytic expression. After insertion of the coefficients a_n and Eq. (A.7) into Eq. (A.3) we find a differential equation for the surface temperature and flux

$$\frac{\mathrm{d}\Delta\tilde{T}(0,\tilde{t})}{\mathrm{d}\tilde{t}} - \Delta\tilde{T}(0,\tilde{t}) = -(\pi\tilde{t})^{-1/2} \tag{A.10}$$

The non-dimensional temperature difference and flux are equal at the surface and solving Eq. (A.10) with the boundary condition $\tilde{\varphi}(0,0)=1$, we obtain:

$$\tilde{\varphi}(0,\tilde{t}) = \exp(\tilde{t}) \times \mathrm{erfc}(\tilde{t}^{1/2}). \tag{A.11}$$

Sometimes the sensor position z is not accurately known, but it may be estimated by the heat flux $\varphi(z,t)$ observed at the end of the gas exposure. With estimates of the soil properties and a reasonable guess of the initial surface heat flux φ_0 we obtain the non-dimensional time $\tilde{t}$ and non-dimensional heat flux at the end of the gas exposure

$\tilde{\varphi}(\tilde{z},\tilde{t})$. The solution must include this reference point—and that condition determines the non-dimensional sensor depth $\tilde{z}$. The method is sketched in Fig. 6: the circles are obtained by three estimates of the surface heat flux, and each of these is part of a solution corresponding to a particular sensor depth. These solutions would end at the same fixed point when plotted in real units, but their excursions would differ slightly. The curve, which best fit the measurements, defines the most likely initial surface flux φ_0 and sensor depth z.

Appendix B

Does the heat of condensation term ΔH_{con} contribute the sensor positions or has the liquid evaporated by then?

The answer to this question depends on atmospheric humidity. In case of small gas concentrations $c \ll 1$, the main aerosol component is condensated air humidity. With the aid of the homogeneous equillibrium assumption we approximate the heat of condensation by

$$\Delta H_{\mathrm{con}} \approx M_{\mathrm{H_2O}} L_{\mathrm{H_2O}} \times \max\left\{0,\ \mathrm{RH} \times P_{\mathrm{sat}}^{\mathrm{H_2O}}(T_{\mathrm{air}}) - P_{\mathrm{sat}}^{\mathrm{H_2O}}(T)\right\} \times P_{\mathrm{air}}^{-1} \qquad \text{(B.1)}$$

where RH is the relative humidity of the air and $P_{\mathrm{sat}}^{\mathrm{H_2O}}(T)$ is the saturation vapour pressure. At small gas concentrations we further approximate the enthalpy deficit by

$$\Delta H \approx (T - T_{\mathrm{air}})\, M_{\mathrm{air}} c_P^{\mathrm{air}} + \Delta H_{\mathrm{con}} \qquad \text{(B.2)}$$

and the significance of the condensation term is seen to be a function of the atmospheric conditions (T_{air}, P_{air}, RH) and the mixture temperature T. The curves in Fig. 7 show the ratio of the two enthalpy terms estimated by the conditions listed in Table 2 as a

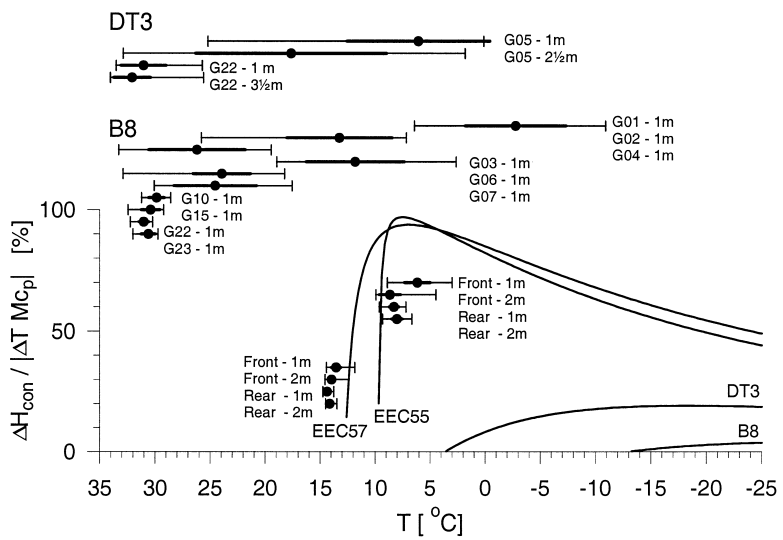

Fig. 7. Ratio of the heat of condensation and the heat associated with the temperature deficit as a function of temperature. Average temperatures are indicated by marker points and the standard deviation and temperature range are indicated by error bars plotted with bold and a thin lines, respectively.

function of mixture temperature. Also shown in the figure are the mean, standard deviation, and range of the selected temperature time series.

The significance of the condensation term ΔH_{con} may be assessed by the curve for the relevant experiment at the local temperature interval. In this way the heat of condensation ΔH_{con} is judged to be very important in EEC55 and irrelevant in B8. In DT3 the condensation seems to have taken place at the G01 mast and in part of the time at G03. The corresponding ΔH_{con} terms were however relatively insignificant because of the large temperature deficits. Furthermore the figure suggests that condensation in EEC57 took place only at the front mast and only in part of the time.

Comments in data reports and log-books suggest that the gas clouds, at least for part of the time, were visible beyond the boundaries suggested by the above analysis. This was probably because the visible fragments were fine filaments of high concentration and low temperature causing temperature fluctuations too rapid to be recorded by thermocouples. It should be remembered that the thermocouple response times were ≈ 1 s and the advection velocities were 2–7 m s^{-1}. In principle this instrumental averaging might have led to too low estimates of the degree of condensation and the (positive) ΔH_{con} term. We do believe this to be no serious error but note that it tends to enhance the deviation from adiabatic mixing, see Fig. 4.

References

[1] D.M. Webber, Report SRD-R243, UK Atomic Energy Authority, Safety and Reliability Directorate, 1983.
[2] R.N. Meroney, D.E. Neff, J. Heat Transfer 108 (1986) 9–15.
[3] M. Ruff, F. Zumsteg, T.K. Fanneløp, J. Hazard. Mater. 19 (1988) 51–68.
[4] H.P. Gröbelbauer, Dissertation, Swiss Federal Institute of Technology, Zürich, 1995.
[5] R.E. Britter, Report CUED/A-Aero/TR-14, Engineering Department, Cambridge University, 1987.
[6] J.P. Kunsch, T.K. Fanneløp, J. Hazard. Mater. 43 (1995) 169–193.
[7] D.M. Webber, S.J. Jones, G.A. Tickle, T. Wren, Report SRD/HSE-R587, UK Atomic Energy Authority, Safety and Reliability Directorate, 1992.
[8] J. Kukkonen, M. Kulmala, J. Nikmo, T. Vesala, D. Webber, T. Wren, Atmos. Environ. 28 (1994) 2763–2776.
[9] C.J. Wheatley, Report SRD/HSE-R410, UK Atomic Energy Authority, Safety and Reliability Directorate, 1987.
[10] M. Nielsen, S. Ott, H.E. Jørgensen, R. Bengtsson, K. Nyrén, S. Winter, D. Ride, C. Jones, J. Hazard. Mater. 56 (1997) 59–105.
[11] D.S. Nielsen, J. Loss Prev. Process Ind. 4 (1991) 236–241.
[12] M. Nielsen, S. Ott, Report R-845(EN), Risø National Laboratory, 1995.
[13] M. Nielsen, J. Loss Prev. Process Ind. 4 (1991) 29–34.
[14] M. Heinrich, R. Scherwinski, Report 123UI00780, TÜV Norddeutchland, Hamburg, 1990.
[15] N.B. Vargaftik, Tables on the Thermophysical Properties of Liquids and Gases in Normal and Dissociated States, Wiley, New York, 1975.
[16] R.P. Koopman, R.T. Cederwall, D.L. Ermak, H.C. Goldwire, W.J. Hogan, J.W. McClure, T.G. McRae, D.L. Morgan, H.C. Rodean, J.H. Shinn, J. Hazard. Mater. 6 (1982) 43–83.
[17] H.C. Goldwire, T.G. McRae, G.W. Johnson, D.L. Hipple, R.P. Koopman, J.W. McClure, L.K. Morris, R.T. Cederwall, Report UCID-20562, US Lawrence Livermore National Laboratory, 1985.
[18] H.S. Carslaw, J.C. Jaeger, Conduction of Heat in Solids, Oxford Univ. Press, 1959.

[19] R.P. Koopman, T.G. McRae, H.C. Goldwire, D.L. Ermak, E.J. Kansa, in: S. Hartwig (Ed.), Heavy Gas and Risk Assessment III, Reidel, 1986.
[20] R.P. Koopman, J. Baker, R.T. Cederwall Jr., H.C. Goldwire, W.J. Hogan, L.M. Kamppinen, R.D. Kiefer, J.W. McClure, T.G. McRae, D.L. Morgan, L.K. Morris, M.W. Spann, C.D. Lind, Report UCID-19075, US Lawrence Livermore National Laboratory, 1982.
[21] M. Nielsen, N.O. Jensen, Report M-2923, Risø National Laboratory, 1991.